Applied Catalysis B: Environmental 333 (2023) 122782

Contents lists available at ScienceDirect

Applied Catalysis B: Environmental

journal homepage: www.elsevier.com/locate/apcatb

Superheterojunction covalent organic frameworks: Supramolecular synergetic charge transfer for highly efficient photocatalytic CO_2 reduction

Shao–Shuai Zhao [a,b], Jun Liang [a,e,*], Duan-Hui Si [a,**], Min-Jie Mao [a], Yuan–Biao Huang [a,c,d,*], Rong Cao [a,b,c,d,*]

[a] State Key Laboratory of Structural Chemistry, Fujian Institute of Research on the Structure of Matter, Chinese Academy of Sciences, Fuzhou 350002, China
[b] School of Physical Science and Technology, ShanghaiTech University, Shanghai 201210, China
[c] University of Chinese Academy of Sciences, Beijing 100049, China
[d] Fujian Science & Technology Innovation Laboratory for Optoelectronic Information of China, Fuzhou 350108, China
[e] School of Chemical Engineering and Technology, Hebei University of Technology, Tianjin 300401, China

ARTICLE INFO

Keywords:
Covalent organic framework
Porphyrin
Charge transfer
Heterojunction
CO_2 photoreduction

ABSTRACT

Photocatalytic conversion of CO_2 into value–added chemicals under visible light irradiation is very appealing but challenging due to the easy recombination of hole–electron pairs in traditional photocatalysts. π–π stacking interactions can be favorable for efficient separation and transfer of photo–irradiated charges to promote photocatalysis, but are rarely studied in crystalline porous frameworks like covalent organic frameworks (COFs). Herein, we report a series of thienothiophenes–porphyrin based 2D COFs, denoted as TT–Por(M)–COF (M = 2 H/Co/Cu/Ni), which show enhanced intralayer and interlayer charge separation and migration due to the donor-acceptor heterojunctions and π–stacked columns. The TT–Por(Co)–COF achieves enhanced CO evolution rate than COF–366–Co without the heterojunctions and π–columns (10.05 mmol g^{-1} h^{-1} versus 7.10 mmol g^{-1} h^{-1}) under visible light irradiation. This work not only shows the important role of π–π stacking interactions of COFs for CO_2 conversion, but also provides insight into the mechanistic aspect for photocatalysis.

1. Introduction

The capture and catalytic conversion of carbon dioxide to value–added chemical feedstocks including CO, CH_4 is of significant importance for the sustainable development of modern society [1–6]. Among the various catalytic conversion approaches, the photocatalytic CO_2 reduction is particularly intriguing in terms of high product selectivity, mild conditions, and clean sunlight as sustainable energy [7–9]. To achieve efficient photocatalytic performance, great efforts have been made to enhance the catalytic reduction of CO_2 via increasing the visible light absorption range and improving the electron–hole separation and migration ability [10–13]. Several strategies including ion doping, heterostructure design, modifying specific morphology structure or controlling crystal plane and defect engineering, have been developed [14–17]. These approaches made substantial contributions to efficient charge separation in inorganic semiconductors such as TiO_2 and ZnO [18–20]. Nevertheless, the large bandgap energies of most inorganic photocatalysts are restricted in the UV absorption range and the poor CO_2 adsorption limited their photocatalytic CO_2 applications. Thus, organic materials including carbon nitride, conjugated microporous polymers (CMPs), and covalent triazine frameworks (CTFs), have emerged as promising photocatalysts for CO_2 reduction owing to their wide visible light absorption range and tunable optoelectronic properties [21–25]. Although amorphous organic polymer photocatalysts with many defects could render rich reactive sites, the photoinduced charges are usually trapped at defect sites and thus fast recombination of the photoexcited electrons and holes easily occurred, which lead to unsatisfied photocatalytic activities.

Recently, porous crystalline covalent organic frameworks (COFs) that are constructed by periodic organic building blocks via covalent bonds have emerged as an important family of polymers, which possess high crystallinity, abundant porosity, and excellent chemical stability [26–30]. COFs have been applied for various fields, including gas storage/separation, heterogeneous catalysis, electrocatalysis, optoelectronics and light

* Corresponding authors at: State Key Laboratory of Structural Chemistry, Fujian Institute of Research on the Structure of Matter, Chinese Academy of Sciences, Fuzhou 350002, China.
** Corresponding author.
E-mail addresses: liangj956@nenu.edu.cn (J. Liang), siduanhui@fjirsm.ac.cn (D.-H. Si), ybhuang@fjirsm.ac.cn (Y. Huang), rcao@fjirsm.ac.cn (R. Cao).

https://doi.org/10.1016/j.apcatb.2023.122782
Received 14 January 2023; Received in revised form 14 March 2023; Accepted 18 April 2023
Available online 19 April 2023

emission [31–35]. Particularly, benefiting from the wide visible–light absorption range and highly crystalline ordered structures, COFs would serve as promising materials for photocatalysis [36–39]. The high surface areas and ordered pores of COFs could provide abundant accessible catalytic sites for substrates. The extensive π–delocalization in the extended COF planes endows them with wide visible–light harvesting and the capability to promote charge transfer. Furthermore, the periodically ordered structure would efficiently transport the photo–irradiated charges to the surface and minimize charge trapping at defect sites, thus suppressing the recombination of electron–hole pairs [40–46]. Moreover, fully coplanar donor–acceptor (D–A) heterojunction structures can be easily constructed in extended π–conjugated COFs skeletons. The periodic vertically oriented D–on–D and A–on–A segregated columns formed a board interface of the periodically ordered heterojunctions, leading to the generation of superheterojunction, which would efficiently make the photogenerated carriers separated and transport to the surface and substrates along the columns (Scheme 1, right bottom) [47–49]. Thus, compared with the amorphous organic polymers, the extended structures both in plane and the π–π stacking direction of COFs should enable fast charge carrier mobility and form a broad interface for charge transfer to restrain the recombination of electron–hole pairs and promote photocatalytic performances. Therefore, it is of significant importance to study on the effect of molecular heterojunction and the periodic π–stacked columnar arrays in COFs for the photoreduction of CO_2.

Metalloporphyrins have been widely used for its light absorption and providing active sites in advanced photocatalytic systems [50,51]. Thienothiophenes (TTs) have been widely applied in organic solar cells because the d–orbitals of sulfur atom can mix well with aromatic π–orbitals and thus give more electrons to acceptor groups [52,53]. Therefore, it can be envisioned that the combination of TT and metalloporphyrin units in 2D COFs would afford expected periodically ordered D–A heterojunction structure and π–columnar arrays. Herein, a series of 2D COFs are constructed by the electron–rich thienothiophene (TT) and electron–acceptor metalloporphyrin (TAPP–2 H/Co/Cu/Ni) units. The direct covalent coupling between TT and TAPP forms a molecular–level heterojunction in the COF skeleton, and the π–stacked columnar arrays between layers are expected to delocalize the charges, suppressing charge recombination (Scheme 1). Photoelectrochemical tests including electrochemical impedance spectroscopy, steady-state and time-resolved photoluminescence spectroscopy verified that the optimal TT–Por(Co)–COF exhibited better photoelectric abilities and had longer–lived charge carriers than that of corresponding COF–366–Co without the D–A heterojunctions and π–columns. Furthermore, transient absorption spectroscopy revealed a longer excited state lifetime and the theoretical calculations proved that the excited electrons were capable to transfer from TT to porphyrin units due to the heterojunction incorporation, and the separation efficiency of electron and hole were also improved with the COF layers increasing from single to triple layers. The optimized TT–Por(Co)–COF shows excellent photocatalytic activity and stability in CO_2 conversion to CO, and the conversion can reach 10.05 mmol h^{-1} g^{-1} under visible light illumination, which is superior to the benchmark COF-366-Co (7.1 mmol h^{-1} g^{-1}). This work demonstrates that developing 2D COFs with D–A heterojunction and electron columns via π–π stacking can be a promising strategy for enhancing photocatalytic CO_2 conversion.

2. Materials and methods

2.1. Materials

Commercially reagents and solvents were used without further purification. Synthesis of the mono-mers can be found in the supplementary data.

2.2. Preparation of TT-Por(Co)-COF

The synthesis of TT-Por(Co)-COF was carried out according to the previously reported protocol with slight modification. A Pyrex tube was charged with 15.8 mg (0.08 mmol) of thieno[3,2-*b*]thiophene-2,5-dicarboxaldehyde (TT), 29.4 mg (0.04 mmol) of TAPP-Co and a solvent mixture of benzyl alcohol, o-dichlorobenzene and 6 M acetic acid (30:10:4 v:v:v, 1.1 mL), and sonication. After freeze-pump-thaw, the tube was sealed and heated to 120 °C for 72 h. The resulting solid was collected by centrifugation and washed with dioxane until the filtrate turned to colorless. After that, the powder was transferred to Soxhlet extractor and thoroughly washed with dioxane (24 h) and acetone (24 h). Finally, the product was evacuated at 120 °C under dynamic vacuum overnight to yield activated sample.

2.3. Characterization

Powder X-ray diffraction (PXRD) patterns were recorded on reflection mode on a Miniflex 600 with Cu Kα. Fourier transform infrared spectra were conducted in VERTEX70 (Bruker). The NMR spectra were measured on an Avance III Bruker Biospin spectrometer. Nitrogen sorption measurements were measured using an ASAP 2460 instrument

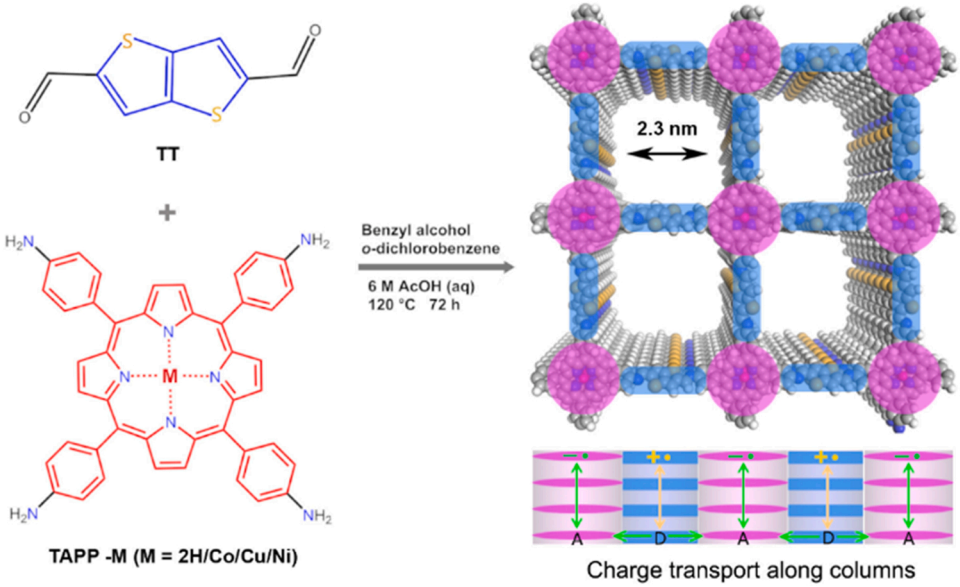

Scheme 1. Schematic synthesis of TT–Por(M)–COF via the condensation of TT and TAPP–M (M = 2 H/Co/Cu/Ni). (Right) Top and side views of the 2D π–stacking structure of the resultant TT–Por(M)–COF (C, gray; N, blue; S, brown; M, pink; H, white). The electron acceptor (A) and donor (D) units are simplified as pink ellipse and blue rectangle. D-A heterojunctions can be formed within single layer of TT–Por(M)–COF. AA columns and DD columns can be formed along one direction, forming superheterojunctions as potential channels for photoinduced charge transfer.

(77 K). Transmission electron microscopy (TEM) and energy-dispersive X-ray (EDX) spectroscopy images were carried out with JEOL-2010 FEI Tecnai G20 field-emission microscope (JEOL, Tokyo, Japan) operated at 200 kV. UV–vis adsorption spectra were recorded on Lambda 950. The photoluminescence (PL) spectra were measured using Fluorescence Spectrometer FS5. The electron spin resonance (EPR) measurements were acquired with Bruker Biospin GMBH. The transient absorption spectra were recorded with HELIOS.

2.4. Photocatalytic reaction of CO_2

The photocatalytic activities of all samples were carried out in a double-walled 180 mL quartz reactor at 25 °C maintained by water bath. A mixed solution of MeCN, H_2O and TEOA (3:1:1, 5 mL) containing photocatalyst (5 mg) and $[Ru(bpy)_3]Cl_2$•6 H_2O (30 mg) was evacuated and purged with CO_2 for several times. The solution was irradiated under a xenon lamp (300 W) with a UV cutoff filter ($\lambda \geq 400$ nm). The gas products were measured using gas chromatography (Agilent 7820 A). The isotope of ^{13}C was analyzed using gas chromatography-mass spectrometry (Shimadzu, GCMS-QP2020).

3. Results and Discussion

3.1. Synthesis and Characterization

The TT and porphyrin based 2D COFs, denoted as TT–Por(M)–COF (M = 2 H, Co, Cu and Ni), were synthesized by the condensation reaction of TT with TAPP–M (M= 2 H, Co, Cu and Ni) under solvothermal conditions (Scheme 1). The crystalline structures of the obtained samples were analyzed by powder X–ray diffraction (PXRD) measurements in combination with Materials Studio and the Pawley refinements calculation. The triclinic *P1* space group for the typical TT–Por(Co)–COF was built with a unit cell parameter of $a = 27.20$ Å, $b = 27.14$ Å, $c = 4.17$ Å, and $\alpha = 111.22°$, $\beta = 79.17°$, $\gamma = 96.46°$. The slight deviations between adjacent layers are energetically favorable. The simulated PXRD patterns reproduced the experimentally observed peaks with unweighted–profile R factor (R_p) = 7.00% and weighted–profile R factor (R_{wp}) = 5.41%, suggesting the validity of the computational model. The intense PXRD peaks at 3.4°, 6.7° and 7.6° for the representative TT–Por(Co)–COF could be assigned to (110), (200) and (020) faces, respectively (Fig. 1a).

These refinements results suggested that there was a channel along *c* axis with a theoretical pore size of 2.3 nm (Scheme 1). Based on the simulated structure, it was found that 2D COFs induced a large electron coupling between the π–orbitals of adjacent layers and facilitated the charge transfer through the preorganized π–pathways. Moreover, the alternately linked metalloporphyrin and TT units form intralayer heterojunctions in COF skeleton, thus these heterojunctions are further arranged in a periodically ordered columnar arrays along the π–stacking direction, which should facilitate the charge carrier transport through the preorganized superheterojunctions (Scheme 1). In addition, the PXRD patterns of all TT–Por(M)–COF materials are very similar, indicating their iso-reticular framework structures (Fig. S1). The chemical structure of the typical sample TT–Por(Co)–COF was confirmed by Fourier–transform infrared (FT–IR) spectroscopy and ^{13}C solid–state nuclear magnetic resonance (^{13}C NMR) spectroscopy. The appearance of

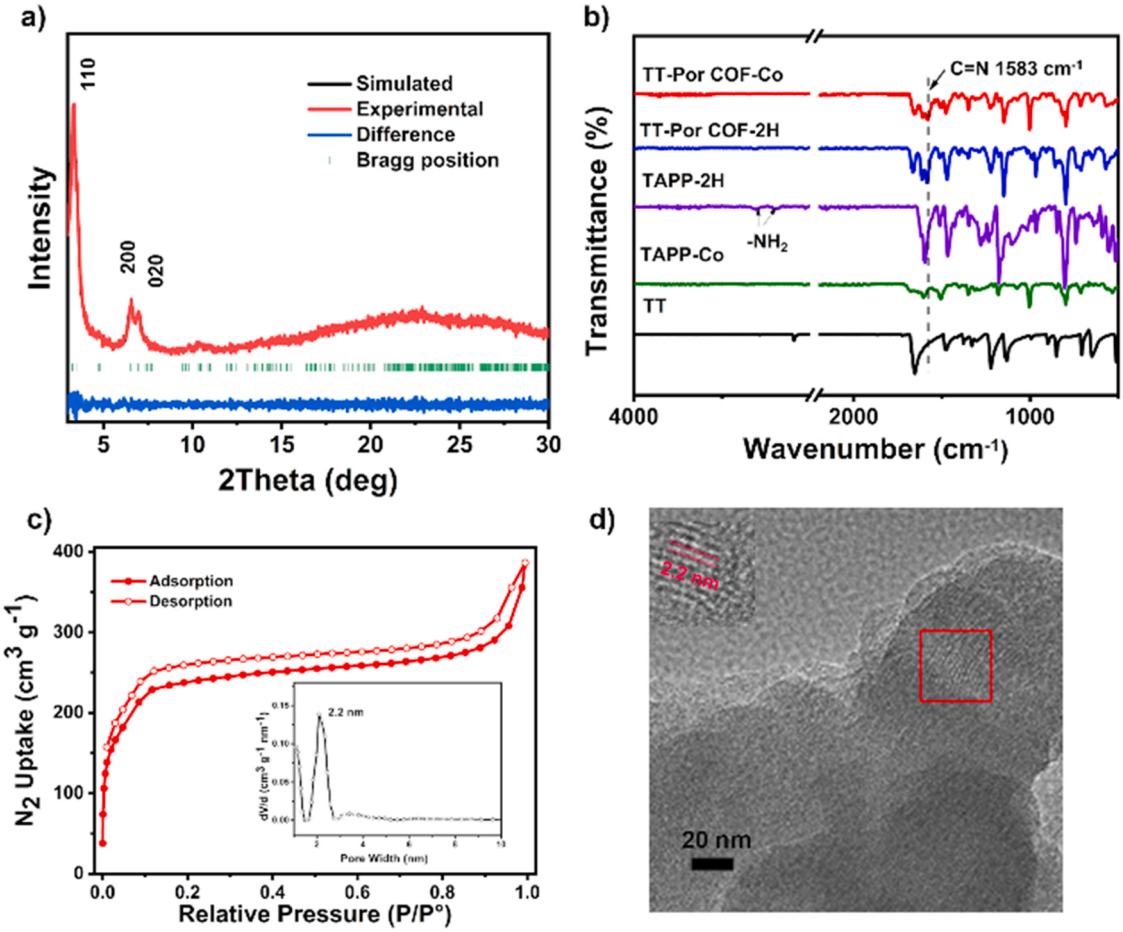

Fig. 1. a) Experimental and simulated PXRD patterns for a staircase arrangement of TT–Por(Co)–COF. b) FT–IR spectra of TT–Por(Co)–COF, TT–Por(2 H)–COF and corresponding TT, TAPP–2 H and TAPP–Co monomers. c) N_2 sorption isotherms of TT–Por(Co)–COF at 77 K and pore–size distribution profile (inset) based on nonlocal density functional theory (NLDFT) calculations. d) TEM images of TT–Por(Co)–COF (insert: HR–TEM image).

1583 cm^{-1} indicated the formation of imine linkages in TT–Por(Co)–COF (Fig. 1b). The formation of imine linkages in the TT–Por(M)–COF was also confirmed by FT–IR (Fig. S2).

Furthermore, the characteristic signal of TT–Por(Co)–COF at 146 ppm was assigned to the C═N bond arising from COF formation in solid state ^{13}C NMR spectrum (Fig. S3). To evaluate the permanent porosity of TT–Por(Co)–COF, N_2 sorption experiments were carried out at 77 K. The Brinauer–Emmett–Teller (BET) surface area of TT–Por(Co)–COF was found to have a BETsurface area of 732 m^2 g^{-1} and pore size distribution cantered at 2.2 nm (Fig. 1**c**), which is well matched with the simulated porous structure (Scheme 1). TT–Por(M)–COF materials had similar porosity properties (pore size about 2.2 nm) due to their isoreticular structures (Fig. S4–S7). The scanning electron microscopy (SEM) image revealed TT–Por(Co)–COF is assembled by small rectangular sheet–shaped crystals (Fig. S8). The high–resolution transmission electron microscopy (HR–TEM) showed the high crystallinity and the lattice fringe spacing of 2.2 nm (Fig. 1d), which was close to the pore size calculated from the nitrogen sorption isotherm (2.2 nm, Fig. 1c) and theoretical value (2.3 nm, Scheme 1) predicted by the structure model. These results confirmed the successful formation of crystalline ordered networks. Furthermore, the energy–dispersive X–ray (EDX) mapping images indicated that C, N, S and Co elements were homogeneously distributed in the whole TT–Por(Co)–COF matrix (Fig. S9). The element analysis (EA) revealed that the contents of S and N were 8.37 and 9.86 wt%, respectively. Moreover, the inductively coupled plasma (ICP) optical emission spectrometry analysis showed that the Co content of TT–Por(Co)–COF was 4.95%. The X–ray photoelectron spectroscopy (XPS) analysis results showed the existence of C, N, S and Co, and the divalent state of the cobalt ion in the porphyrin pocket of TT–Por(Co)–COF (Fig. S10).

To further examine the coordination configuration of single Co sites, X–ray absorption near–edge structure (XANES) and extended X–ray absorption fine structure (EXAFS) measurements were performed [56, 57]. A pre–edge peak at 7715 eV observed in the Co *K–edge* XANES spectrum of TT–Por(Co)–COF could be assigned to a shake down satellite involving the 1 s→4p transition (Fig. 2a), and the pre-edge peak for TT–Por(Co)–COF located between those of CoO and Co foil, indicating that the electron structure of TT–Por(Co)–COF is between Co (II) and Co (0). According to the results of the Co *K*–edge EXAFS analysis, no obvious Co–Co or Co–O signals showed up in TT–Por(Co)–COF, indicating the absence of Co–derived metallic Co or CoO clusters/particles (Fig. 2b). The coordination structure of TT–Por(Co)–COF was analysed by fitting the k^3–weighted Fourier–transform EXAFS spectra with the TCPP–Co (Fig. S11). These results confirm the atomic dispersion of Co–N_4 species in the porphyrin pocket.

3.2. Photoelectric Properties

To elucidate the semiconductor character and possibility for photocatalysis, UV–vis–NIR diffuse reflectance spectroscopy (DRS) associated with Mott–Schottky measurements were carried out to determine the band positions. The as-synthesized TT–Por(M)–COF showed a broad visible light absorption (Fig. 2c, Fig. S12), and the band gap of TT–Por (M)–COF (M = 2 H/Co/Cu/Ni) were determined to be 1.69, 1.57, 1.78

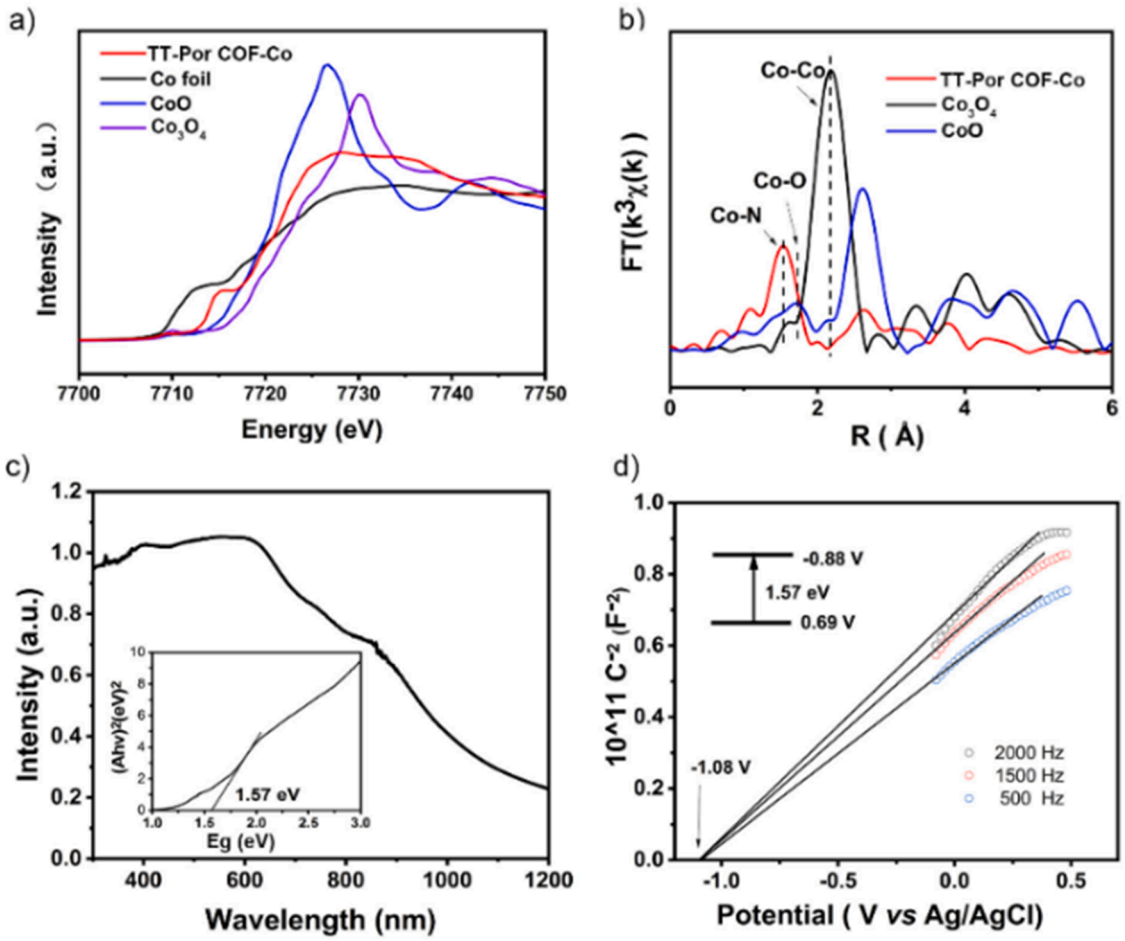

Fig. 2. a) Normalized Co K–edge XANES spectra of Co foil, CoO, Co_3O_4 and TT–Por(Co)–COF. b) Fourier transform EXAFS spectra of the Co foil, CoO and TT–Por (Co)–COF. c) Solid–state UV–vis–NIR DRS of TT–Por(Co)–COF (insert Tauc plot of TT–Por(Co)–COF). d) Mott–Schottky plots of TT–Por(Co)–COF in 0.2 M Na_2SO_4 aqueous solution (pH = 6.8).

and 1.82 eV according to Tauc plot (Fig. 2c and Fig. S13–S15), respectively. Among them, the narrowest band gap for TT–Por(Co)–COF stood out due to its narrowest band gap (1.57 eV), indicating possibility for visible light absorption to promote photocatalysis. According to the Mott–Schottky experiments (Fig. 2d), TT–Por(Co)–COF was a n–type semiconductor due to the positive slopes of the C^{-2} values and the flat band potential was determined to −0.88 V (V vs. V_{NHE}). The relative valence band maximum (VBM) and conduction band minimum (CBM) potential of TT–Por(Co)–COF were 0.69 V and −0.88 V (V vs. V_{NHE}), respectively. The CBM of TT–Por(Co)–COF was negative than the standard reduction potential of CO_2 to CO (–0.52 V vs. V_{NHE}), indicating the theoretical feasibility for photocatalytic CO_2 reduction to CO. Besides, the results of Mott–Schottky measurements of TT–Por(M)–COF (M = 2 H/Cu/Ni) and corresponding COF–366–Co with poor D–A heterojunction determined the conduction band positions to be –0.90, –0.89, −0.72 V and −0.85 V (V vs. V_{NHE}), respectively (Fig. S17–S20). Thus, the band structure of these materials theoretically fulfilled the redox potential of photocatalytic CO_2 reduction to CO [58]. To gain insight into the electron transfer process in these materials, the electrochemical impedance spectroscopy measurements were carried out. The semicircle with much smaller diameter in the Nyquist plot of TT–Por(Co)–COF revealed its lower charge transfer resistance than other TT–Por(M)–COF materials (Fig. S21). Furthermore, the photocurrent measurement results indicated that TT–Por(Co)–COF had a higher photocurrent response (Fig. S22). The powder pellet two-electrode method was performed to further investigate the conductivity of TT–Por(Co)–COF. The bulk conductivity of TT–Por(Co)–COF was calculated up to 1.36×10^{-8} S m^{-1} at 298 K, which was higher than that of COF-366-Co (6.5×10^{-9} S m^{-1}) (Fig. S23) [54]. The carrier mobility (μ) of TT–Por(Co)–COF was calculated to 0.16 cm^2 V^{-1} s^{-1}, also higher than that of COF-366-Co (0.06 cm^2 V^{-1} s^{-1}), according to the space charge-limited current (SCLC) model (Fig. S24) [55]. All these results suggested that TT–Por(Co)–COF might show superior photocatalysis performance.

3.3. Photocatalytic performance

The photocatalytic CO_2 reduction activity of these COFs were subsequently investigated using $[Ru(bpy)_3]Cl_2{\cdot}6\,H_2O$ (bpy = 2,2′–bipyridine) as photosensitizer and triethanolamine (TEOA) as electron sacrificial reagent in acetonitrile/H_2O solution. Among all the photocatalysts, TT–Por(Co)–COF showed the highest CO evolution yield of 31.8 mmol g^{-1} under visible light irradiation after 2 h, which was obviously higher than that of TT–Por(Cu)–COF (0.2 mmol g^{-1}) and TT–Por(Ni)–COF (0.4 mmol g^{-1}) (Fig. 3a). The different CO_2 reduction performance of TT–Por(M)–COF materials indicated the important role of metal centers in the frameworks. The superior CO yield achieved by TT–Por(Co)–COF could be related to its relatively narrow band gap (1.57 eV). It should be noted that both photosensitizer and electron sacrificial reagent are necessary in this system. Further, the time–dependent evolution of CO over TT–Por(Co)–COF was investigated. As shown in Fig. 3b, TT–Por(Co)–COF showed excellent photocatalysis performance in CO_2 conversion with a total amount of CO as

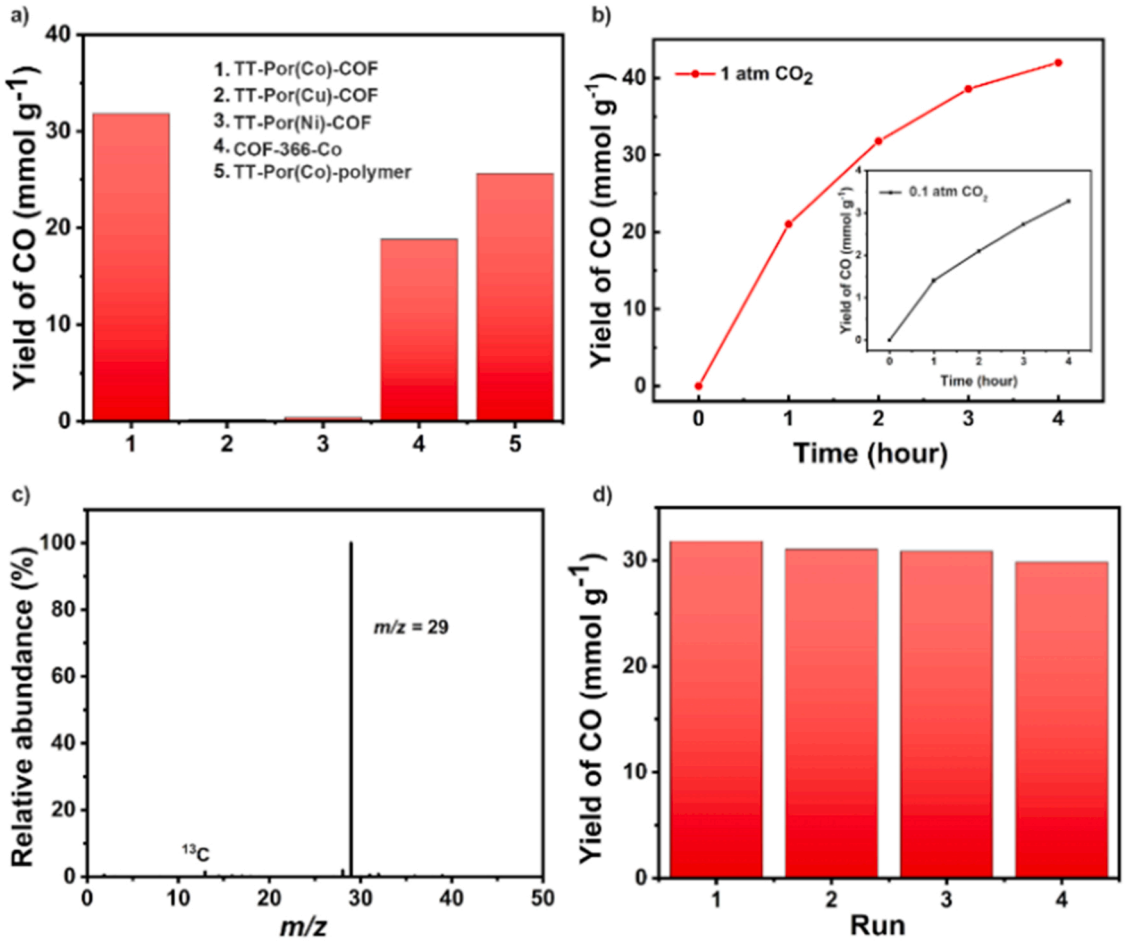

Fig. 3. a) Photocatalytic performance over different catalysts after 2 h. b) Time–dependent evolutions of CO over TT–Por(Co)–COF (insert 0.15 atm CO_2 diluted with N_2). c) Mass spectrum of ^{13}CO produced from the photocatalytic reduction of $^{13}CO_2$ over TT–Por(Co)–COF. d) Stability tests of TT–Por(Co)–COF for photoreduction of CO_2. Until otherwise stated, all experiments are conducted with $[Ru(bpy)_3]Cl_2{\cdot}6\,H_2O$ (bpy = 2,2′–bipyridine) as the photosensitizer and triethanolamine (TEOA) as the electron sacrificial reagent at 298 K.

42 mmol g^{-1} (10.5 mmol g^{-1} h^{-1}) during 4 h reaction period (Fig. S25), which was higher than those of other COFs studied to date (Table S1).

It should be noted that when COF–366–Co was used as the photocatalyst, an apparent lower CO evolution yield of 18.8 mmol g^{-1} was observed (Fig. 3a). COF–366–Co showed lower CO_2 reduction activity than TT–Por(Co)–COF, indicating the importance of superheterojunctions in the framework for promoting electron-hole separation during catalysis. To investigate the effect of crystallinity of TT–Por (Co)–COF on the catalytic performance, amorphous TT–Por(Co)–polymer was prepared under similar synthetic conditions without acetic acid. A much lower yield than that of TT–Por(Co)–COF (25.6 versus 31.8 mmol g^{-1}) was also observed (Fig. 3a), which strongly highlighted the importance of the periodic π–stacked columnar arrays in TT–Por (Co)–COF for efficient charge transfer and boosting photocatalytic CO_2 reduction. When the photocatalytic reaction was conducted in the diluted CO_2 (15% CO_2 and 85% N_2), 3.2 mmol g^{-1} of CO was achieved in

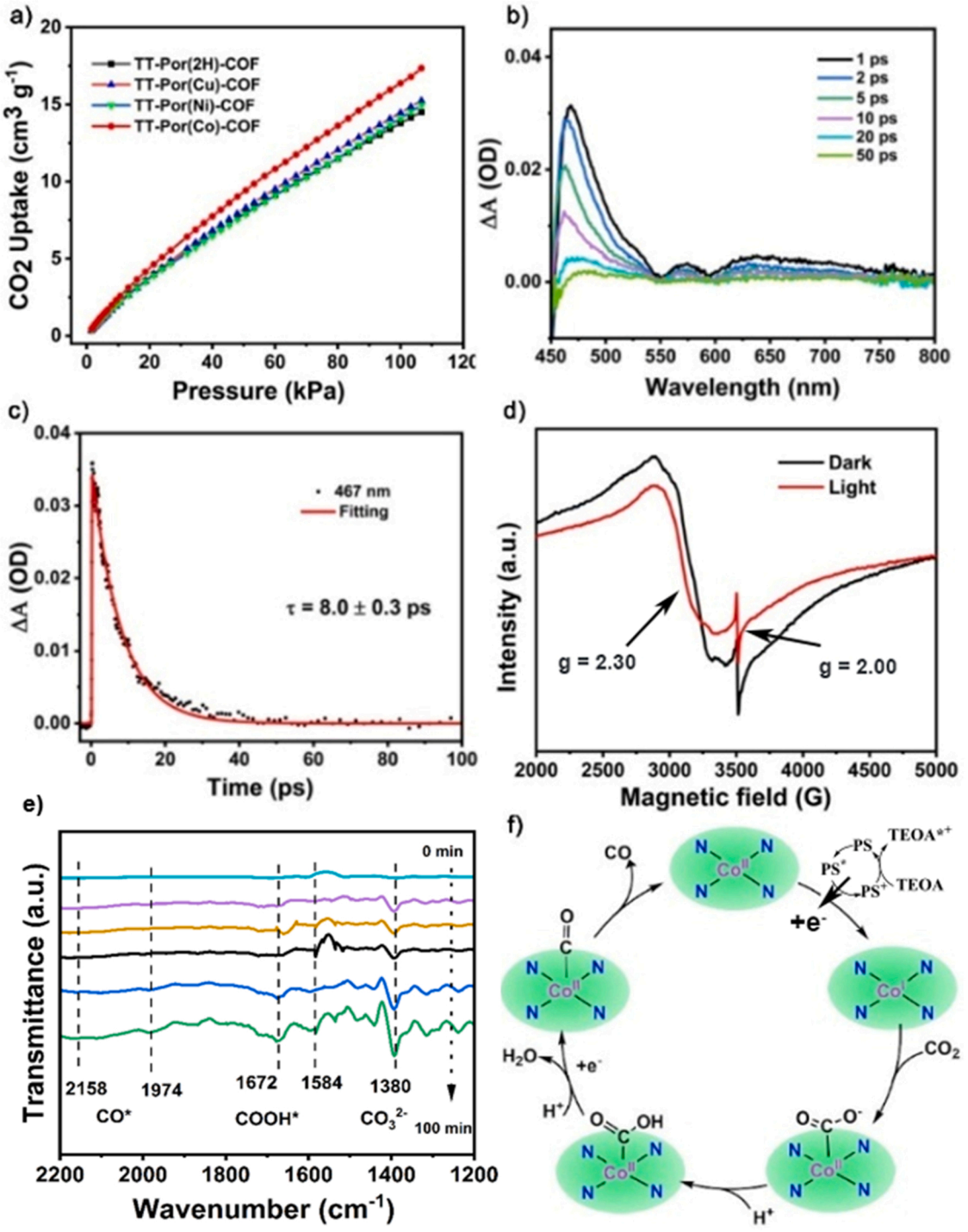

Fig. 4. a) CO_2 adsorption curves of TT–Por(M)–COF measured at 298 K up to 1 bar. b) Femtosecond transient absorption spectra of TT–Por(Co)–COF in DMF. c) Time profile of the transient absorption band of TT–Por(Co)–COF at 467 nm. d) EPR spectra of TT–Por(Co)–COF in dark and under light irradiation. e) In–situ diffuse reflectance infrared Fourier transform spectroscopy (DRIFTS) for the photocatalytic reduction of CO_2 over TT–Por(Co)–COF. f) The proposed mechanism over TT–Por (Co)–COF for the CO_2 photoreduction reaction.

a 4 h reaction (Fig. 3b insert), which was comparable to those of reported photocatalytic systems (Table S2).

To identify the key factors for CO_2 photoconversion, a series of control experiments were performed with TT–Por(Co)–COF (Fig. S26). When the CO_2 reduction reaction was conducted in the dark, no gas or liquid products were detected, indicating that CO_2 conversion was initiated by light irradiation. In the absence of sacrificial agent, photocatalyst or photosensitizer, only very small amount of CO was detected. When the photocatalytic system was carried out in the Ar atmosphere, little H_2 and no CO were detected, suggesting that the CO originates from CO_2. To confirm this, an isotope experiment was also carried out. An intense peak at $m/z = 29$ and the fragment (^{13}C at $m/z = 13$) were found, indicating high accordance with the standard mass spectrum of ^{13}CO (Fig. 3c). These solid evidences confirmed that the produced ^{13}CO indeed originated from $^{13}CO_2$ in the CO_2 photoreduction process over TT–Por(Co)–COF.

Additionally, recyclable experiments were carried out to investigate the stability of TT–Por(Co)–COF, and the CO evolution remained 29.8 mmol g^{-1} (93% with respect to the value of initial run) after four runs (Fig. 3d). Moreover, the FT–IR spectra, PXRD, and SEM image of TT–Por(Co)–COF after photocatalysis remained the same as the pristine one, which suggested the excellent photostability of as prepared TT–Por (Co)–COF (Fig. S27–29). Furthermore, the XPS measurements of the sample confirmed that the oxidation state of Co remained at + 2 after the catalysis experiments and Fourier transform EXAFS spectra confirmed that no Co–derived metallic Co or CoO clusters/particles appeared (Fig. S30–31). These results indicated that the photocatalytic CO_2 reduction was mainly contributed by the intrinsic networks of TT–Por(Co)–COF, rather than Co/CoO nanoparticles reduced from cobalt porphyrin.

3.4. Mechanism for Photocatalytic CO_2 Reduction

To get insight into the good performance of TT–Por(Co)–COF for photocatalytic CO_2 reduction, the CO_2 sorption isotherms were collected at 298 K up to 1 bar. The results indicated that TT–Por(Co)–COF had a higher CO_2 uptake value (17 cm^3 g^{-1}) than that of TT–Por(2 H)–COF (14 cm^3 g^{-1}) at 106 kPa (Fig. 4a) [59,60]. To investigate the electron transfer behavior, the steady–state photoluminescence (PL) spectroscopy and time resolved PL decay spectroscopy of TT–Por(Co)–COF were conducted. As shown in Fig. S32, the PL intensity of excited $[Ru(bpy)_3]^{2+}$ was gradually quenched with the addition of TT–Por(Co)–COF, which indicated the photo excited electrons were transferred from $[Ru(bpy)_3]^{2+}$ to COF skeletons. Further, the plot for the PL intensities versus the addition of TT–Por(Co)–COF turned out to be upward curvature as fitted with the Stern–Volmer equation, indicating that the PL of $[Ru(bpy)_3]^{2+}$ was static–quenched by TT–Por(Co)–COF (Fig. S33) [61]. Compared with the addition of COF–366–Co, the addition of TT–Por (Co)–COF obviously weakened the PL intensity, demonstrating that the superheterojunctions in COF was favorable for efficient charge transfer, which might explain the higher photocatalysis activity (Fig. S34). According to the PL decay spectroscopy, the PL lifetime decreased from 356 ns to 328 ns and 273 ns for $[Ru(bpy)_3]^{2+}$, TT–Por(2 H)–COF and TT–Por(Co)–COF, respectively (Fig. S35–37). These results suggested that the photo excited electrons were transferred from $[Ru(bpy)_3]^{2+}$ to COF skeleton, and eventually migrated to active cobalt sites. Furthermore, the lifetime (273 ns) of TT–Por(Co)–COF was shorter than that of COF–366–Co (290 ns) (Fig. S38), indicating that the D–A heterojunction structures indeed facilitated the charge separation of the photoexcited TT–Por(Co)–COF.

To gain a deeper understanding of photoexcited charge separation in TT–Por(Co)–COF, we resorted to ultrafast transient absorption (TA) spectroscopy [62]. According to the detailed spectral changes taking place on different time scales, the observed positive features at 467 nm in the TA spectra of TT–Por(Co)–COF could be considered as excited state absorption (ESA), which was attributed to cobalt porphyrin radical anion ($CoPor^{\blacksquare -}$) (Fig. 4b) [63]. Upon excited at 375 nm, the increasing TA spectra in 0–380 fs is originated from the light absorption directly coupled with charge dissociation to generate free charges (Fig. S39) [64]. The decay of the ESA signal at 467 nm was fitted and the lifetime of $CoPor^{\blacksquare -}$ of TT-Por(Co)-COF was calculated to be 8.0 ± 0.3 ps (Fig. 4c), which was longer than that of COF-366-Co (7.1 ± 0.4 ps) (Fig. S40–41). Conventionally, a longer excited state lifetime decreased the probability of electron–hole recombination, which was a key process in real photocatalysis system, explaining the higher photocatalytic performance of TT–Por(Co)–COF [65].

After verifying the charge transfer process from $[Ru(bpy)_3]^{2+}$ to the cobalt porphyrin, to gain more information on reaction centers, in situ electron spin resonance (EPR) measurements were further conducted to obtain the information on spin states of cobalt ions in TT-Por(Co)-COF (Fig. 4d). The EPR spectrum of TT–Por(Co)–COF showed a strong signal at g = 2.30 under dark condition due to unpair electrons, and the weakened EPR signal upon light irradiation indicated some of the high–spin–state Co (II) could be reduced to low–spin–state Co (I) [66]. Furthermore, in situ XPS were performed over TT–Por(Co)–COF to show that Co (II) has lower binding energy with light (794.32 eV for $2p_{3/2}$ and 778.57 eV for $2p_{1/2}$) than that in dark (794.59 eV for $2p_{3/2}$ and 778.98 eV for $2p_{1/2}$), which revealed the existence of photo–induced low–spin–state Co (I) (Fig. S42). While the binding energy of sulfur in TT–Por(Co)–COF exhibited a higher binding energy after light irradiation, indicating that the photogenerated electrons were transferred to porphyrin units and holes were transported to thienothiophene units (Fig. S43). Co 2p XPS spectra were collected and compared for TAPP–Co, TT–Por(Co)–COF and COF–366–Co. TT–Por(Co)–COF showed a lower binding energy than that of TAPP–Co and COF–366–Co, indicating that the Co (II) centers of TT–Por(Co)–COF had microenvironment with higher electron intensities (Fig. S44). Therefore, we speculated that the incorporation of heterojunction in COF skeletons could promote the Co (II) photoreduction to Co (I), and enhance the interactions between the Co species and absorbed CO_2 molecules.

Moreover, we also employed in–situ diffuse reflectance infrared Fourier transform spectroscopy (DRIFTS) to confirm reaction intermediates during the CO_2 photoreduction process (Fig. 4e). In the spectra collected during light irradiation, the main intermediate peaks of this process at 1584 cm^{-1} and 1672 cm^{-1} increased over the irradiation time, which can be assigned to the asymmetric stretching vibrations of COOH* and COO^- species, respectively. The FTIR bands at 1974 cm^{-1} are attributed to linearly adsorbed CO. Subsequently, the adsorbed *CO molecules could be readily desorbed from the photocatalyst, as indicated by the peak at 2158 cm^{-1}. [66–68]. Based on these results, a proposed mechanism over TT–Por(Co)–COF for the CO_2 photoreduction reaction can be partly illustrated in Fig. 4f. Upon the photo irradiation, $[Ru(bpy)_3]^{2+}$ was excited, and the photogenerated electrons were then transferred to TT–Por(Co)–COF. The free charges could be generated, separated, and retained in the donor and acceptor π–columns. The Co (II) species maintained the circulation of Co (II) and Co (I) by the photogenerated electrons, and the CO_2 molecules were activated by Co (I) species, realizing the CO_2 conversion to CO.

To clarify how the intralayer heterojunctions and ordered columnar arrays affect the photocatalytic performance, density functional theory (DFT) and time–dependent density functional theory (TD–DFT) calculations were conducted by VASP and Gaussian16 software, respectively (Fig. 5) [69,70]. To explore the role of D–A heterojunctions in COF, the models of TT–Por(Co)–COF (double layers) and COF–366–Co (double layers) were constructed, and the excitation and the corresponding oscillator strengths of 240 excited states were investigated. As shown in Table S3-S4, the maxima of oscillator strengths of TT–Por(Co)–COF and COF–366–Co are S_0–S_{142} and S_0–S_{158}, respectively. Their corresponding optical absorptions were located at 436 nm and 482 nm, which agreed with the experimental absorption value. The distribution of electron and hole of S_{142} state in TT–Por(Co)–COF indicated that excited electrons tend to transfer to metalloporphyrin units, while holes could migrated to

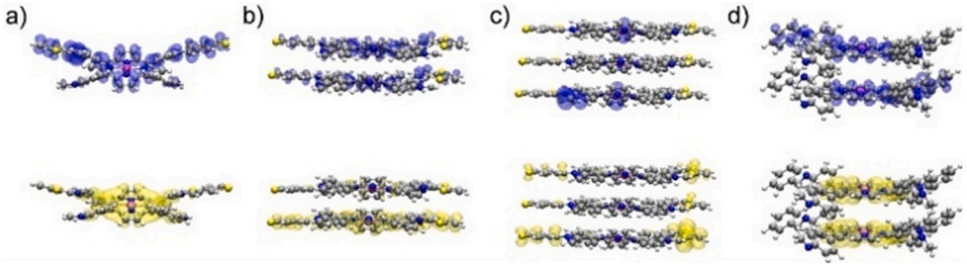

Fig. 5. The electron–hole distribution in the excited state of different TT–Por(Co)–COF models: a) the S_{80} state of single layer, b) the S_{142} state of two layers, and c) the S_{119} state of three layers. d) The electron–hole distribution in the S_{158} state of COF–366–Co models (blue and yellow color represent electrons and holes respectively).

TT units (Fig. 5b). In contrast, the excited electrons and holes were almost overlapped and evenly distributed in the COF–366–Co fragments, causing a poor charge separation and a fast electron–hole recombination (Fig. 5d). The separation efficiency of electron and hole was further revealed by hole delocalization index (HDI) and electron delocalization index (EDI) in quantify, which was explained in detail in supporting information. The HDI (or EDI) is smaller, suggesting the higher delocalization of holes (or electrons). The HDI and EDI of TT–Por (Co)–COF are 2.28 and 2.08, which were obviously smaller than that of COF–366–Co (2.39 and 2.37, Table S5). Thus, these results suggested the D–A heterojunctions in TT–Por(Co)–COF truly promoted the intralayer electron transfer, which was in accordance with the photocatalytic CO_2 reduction performance.

Furthermore, to elucidate the mechanism of charge transfer in π columnar arrays, we built the models of TT–Por(Co)–COF with different layers (single, double and triple layers) (Fig. 5). With the number of COF layers increases, excited electrons and holes tended to separate and migrate to different parts of COF skeleton, which was confirmed by ***t*** index. It indicated that the separation of holes and electrons were more sufficient with the increasing of ***t*** index value. The ***t*** of single layer, double layers and triple layers were –2.196, –0.795 and 7.512, respectively, which implied the separation efficiency of holes and electrons of COF were enhanced by the ordered π columnar arrays. And thus TT–Por (Co)–COF displayed higher photoactivity of CO_2 reduction in comparison with the COF-366(Co) and amorphous TT–Por(Co)–polymer.

4. Conclusion

In conclusion, we have reported a series of 2D COFs, TT–Por(M)–COF (M= 2 H/Co/Cu/Ni) prepared by the condensation of thienothiophene and metalloporphyrin as functional monomers. Notably, the closely stacked 2D TT–Por(Co)–COF featured with ordered D–A heterojunction structure and self–sorted π columnar arrays achieved a CO production rate of 10.05 mmol g^{-1} h^{-1}. From the theoretical calculations and transient absorption spectroscopy, the excellent photocatalytic performance could be attributed to rapid charge separation originated from intralayer heterojunction structure and exceptional long–term charge retention caused by electron and hole columnar arrays. These results suggest that superheterojunctions in COFs are promising for boosting photoenergy conversion processes in photocatalytic systems.

CRediT authorship contribution statement

Shao-shuai Zhao: Conceptualization, Investigation, Writing – original draft. **Jun Liang**: Validation, Writing – review & editing. **Duan-Hui Si**: Software, Validation. **Min-Jie Mao**: Validation. **Yuan-Biao Huang**: Conceptualization, Writing – review & editing. **Rong Cao**: Conceptualization, Supervision, Funding acquisition.

Declaration of Competing Interest

The authors declare that they have no known competing financial interests or personal relationships that could have appeared to influence the work reported in this paper.

Data Availability

Data will be made available on request.

Acknowledgments

We acknowledge the financial support from the National Key Research and Development Program of China (2018YFA0208600, 2018YFA0704502), NSFC (U22A20436, 22071245, 22201286, 22033008 and 22220102005), and Fujian Science & Technology Innovation Laboratory for Optoelectronic Information of China (2021ZZ103).

Appendix A. Supporting information

Supplementary data associated with this article can be found in the online version at doi:10.1016/j.apcatb.2023.122782.

References

[1] Y.Y. Birdja, E. Perez-Gallent, M.C. Figueiredo, A.J. Gottle, F. Calle-Vallejo, M.T. M. Koper, Advances and challenges in understanding the electrocatalytic conversion of carbon dioxide to fuels, Nat. Energy 4 (9) (2019) 732–745.
[2] L. Zou, R.J. Sa, H.W. Lv, H. Zhong, R.H. Wang, Recent advances on metalloporphyrin-based materials for visible-light-driven CO_2 reduction, Chemsuschem 13 (2020) 6124–6140.
[3] S.N. Habisreutinger, L. Schmidt-Mende, J.K. Stolarczyk, Photocatalytic Reduction of CO_2 on TiO_2 and Other Semiconductors, Angew. Chem. Int. Ed. 52 (29) (2013) 7372–7408.
[4] W. Wang, S.P. Wang, X.B. Ma, J.L. Gong, Recent advances in catalytic hydrogenation of carbon dioxide, Chem. Soc. Rev. 40 (7) (2011) 3703–3727.
[5] X. Zhang, R. Sa, F. Zhou, Y. Rui, R. Liu, Z. Wen, R. Wang, Metal-organic framework-derived cus nanocages for selective CO_2 electroreduction to formate, CCS Chem. 3 (12) (2021) 101–109.
[6] H. Lyu, H. Li, N. Hanikel, K. Wang, O.M. Yaghi, Covalent organic frameworks for carbon dioxide capture from air, J. Am. Chem. Soc. 144 (2022) 12989–12995, 1-109.
[7] H. Rao, L.C. Schmidt, J. Bonin, M. Robert, Visible-light-driven methane formation from CO_2 with a molecular iron catalyst, Nature 548 (2017) 74–77.
[8] X. Li, J.G. Yu, M. Jaroniec, X.B. Chen, Cocatalysts for selective photoreduction of CO_2 into solar fuels, Chem. Rev. 119 (6) (2019) 3962–4179.
[9] O. Ola, M.M. Maroto-Valer, Review of material design and reactor engineering on TiO_2 photocatalysis for CO_2 reduction, J. Photochem. Photobiol. C. -Photochem. Rev. 24 (2015) 16–42.
[10] Y. Pan, Y. Qian, X. Zheng, S.-Q. Chu, Y. Yang, C. Ding, X. Wang, S.-H. Yu, H.-L. Jiang, Precise fabrication of single-atom alloy co-catalyst with optimal charge state for enhanced photocatalysis, Natl. Sci. Rev. 8 (1) (2021) nwaa224.
[11] H. Tong, S.X. Ouyang, Y.P. Bi, N. Umezawa, M. Oshikiri, J.H. Ye, Nano-photocatalytic materials: possibilities and challenges, Adv. Mater. 24 (2) (2012) 229–251.

[12] W.G. Tu, Y. Zhou, Z.G. Zou, Photocatalytic conversion of CO_2 into renewable hydrocarbon fuels: state-of-the-art accomplishment, challenges, and prospects, Adv. Mater. 26 (27) (2014) 4607–4626.

[13] Z. Wang, C. Li, K. Domen, Recent developments in heterogeneous photocatalysts for solar-driven overall water splitting, Chem. Soc. Rev. 48 (7) (2019) 2109–2125.

[14] J.G. Hou, S.Y. Cao, Y.Q. Sun, Y.Z. Wu, F. Liang, Z.S. Lin, L.C. Sun, Atomically thin mesoporous In_2O_3-x/In_2S_3 lateral heterostructures enabling robust broadband-light photo-electrochemical water splitting, Adv. Energy Mater. 8 (9) (2018) 9.

[15] J. Jiang, K. Zhao, X.Y. Xiao, L.Z. Zhang, Synthesis and facet-dependent photoreactivity of BiOCl single-crystalline nanosheets, J. Am. Chem. Soc. 134 (10) (2012) 4473–4476.

[16] R. Shi, H.F. Ye, F. Liang, Z. Wang, K. Li, Y.X. Weng, Z.S. Lin, W.F. Fu, C.M. Che, Y. Chen, Interstitial P-doped CdS with long-lived photogenerated electrons for photocatalytic water splitting without sacrificial agents, Adv. Mater. 30 (6) (2018) 6.

[17] H.L. Wang, L.S. Zhang, Z.G. Chen, J.Q. Hu, S.J. Li, Z.H. Wang, J.S. Liu, X.C. Wang, Semiconductor heterojunction photocatalysts: design, construction, and photocatalytic performances, Chem. Soc. Rev. 43 (15) (2014) 5234–5244.

[18] M. Nolan, A. Iwaszuk, A.K. Lucid, J.J. Carey, M. Fronzi, Design of novel visible light active photocatalyst materials: surface modified TiO_2, Adv. Mater. 28 (27) (2016) 5425–5446.

[19] S. Sakthivel, B. Neppolian, M.V. Shankar, B. Arabindoo, M. Palanichamy, V. Murugesan, Solar photocatalytic degradation of azo dye: comparison of photocatalytic efficiency of ZnO and TiO_2, Sol. Energy Mater. Sol. Cells 77 (1) (2003) 65–82.

[20] Y.H. Sang, Z.H. Zhao, M.W. Zhao, P. Hao, Y.H. Leng, H. Liu, From UV to near-infrared, WS2 nanosheet: a novel photocatalyst for full solar light spectrum photodegradation, Adv. Mater. 27 (2) (2015) 363–369.

[21] C.H. Dai, B. Liu, Conjugated polymers for visible-light-driven photocatalysis, Energy Environ. Sci. 13 (1) (2020) 24–52.

[22] L.L. Duan, L. Wang, F.S. Li, F. Li, L.C. Sun, Highly efficient bioinspired molecular ru water oxidation catalysts with negatively charged backbone ligands, Acc. Chem. Res. 48 (7) (2015) 2084–2096.

[23] R. Li, W. Zhang, K. Zhou, Metal-organic-framework-based catalysts for photoreduction of CO_2, Adv. Mater. 30 (35) (2018) 31.

[24] G.X. Zhao, H. Pang, G.G. Liu, P. Li, H.M. Liu, H.B. Zhang, L. Shi, J.H. Ye, Co-porphyrin/carbon nitride hybrids for improved photocatalytic CO_2 reduction under visible light, Appl. Catal. B Environ. 200 (2017) 141–149.

[25] H. Zhong, Z.X. Hong, C. Yang, L.Y. Li, Y.S. Xu, X.C. Wang, R.H. Wang, A covalent triazine-based framework consisting of donor-acceptor dyads for visible-light-driven photocatalytic CO_2 reduction, Chemsuschem 12 (19) (2019) 4493–4499.

[26] S.Y. Ding, W. Wang, Covalent organic frameworks (COFs): from design to applications, Chem. Soc. Rev. 42 (2) (2013) 548–568.

[27] S. Talekar, Y. Kim, Y. Wee, J. Kim, De novo synthesis of enzyme-embedded covalent organic frameworks (COFs) using deep eutectic solvent: Pushing the COF limits, Chem. Eng. J. 456 (2023), 141058.

[28] S.S. Zhao, X.-P. Guo, X.-H. Pan, Y.B. Huang, R. Cao, An “all in one” strategy to boost antibacterial phototherapy via porphyrin and boron dipyrromethenes based covalent organic framework, Chem. Eng. J. 457 (2023), 141017.

[29] Y. Yang, G. Li, D. Ouyang, Z. Cai, Z. Lin, Dual-activation interfacial polymerization based anionic covalent organic framework nanofiltration membrane for high-flux dye separation, Chem. Eng. J. 456 (2023), 141008.

[30] L.-J. Gong, L.-Y. Liu, S.-S. Zhao, S.-L. Yang, D.-H. Si, Q.-J. Wu, Q. Wu, Y.-B. Huang, R. Cao, Rapid charge transfer in covalent organic framework via through-bond for enhanced photocatalytic CO_2 reduction, Chem. Eng. J. (2023), 141360.

[31] H. Furukawa, O.M. Yaghi, Storage of hydrogen, methane, and carbon dioxide in highly porous covalent organic frameworks for clean energy applications, J. Am. Chem. Soc. 131 (25) (2009) 8875–8883.

[32] L. Chen, K. Furukawa, J. Gao, A. Nagai, T. Nakamura, Y.P. Dong, D.L. Jiang, Photoelectric covalent organic frameworks: converting open lattices into ordered donor-acceptor heterojunctions, J. Am. Chem. Soc. 136 (28) (2014) 9806–9809.

[33] Q.R. Fang, S. Gu, J. Zheng, Z.B. Zhuang, S.L. Qiu, Y.S. Yan, 3D microporous base-functionalized covalent organic frameworks for size-selective catalysis, Angew. Chem. Int. Ed. 53 (11) (2014) 2878–2882.

[34] S. Lin, C.S. Diercks, Y.B. Zhang, N. Kornienko, E.M. Nichols, Y.B. Zhao, A.R. Paris, D. Kim, P. Yang, O.M. Yaghi, C.J. Chang, Covalent organic frameworks comprising cobalt porphyrins for catalytic CO_2 reduction in water, Science 349 (6253) (2015) 1208–1213.

[35] H.M. Ding, J. Li, G.H. Xie, G.Q. Lin, R.F. Chen, Z.K. Peng, C.L. Yang, B.S. Wang, J. L. Sun, C. Wang, An AIEgen-based 3D covalent organic framework for white light-emitting diodes, Nat. Commun. 9 (2018) 7.

[36] M. Lu, J. Liu, Q. Li, M. Zhang, M. Liu, J.L. Wang, D.Q. Yuan, Y.Q. Lan, Rational design of crystalline covalent organic frameworks for efficient CO_2 photoreduction with H_2O, Angew. Chem. Int. Ed. 58 (36) (2019) 12392–12397.

[37] H. Wang, H. Wang, Z.W. Wang, L. Tang, G.M. Zeng, P. Xu, M. Chen, T. Xiong, C. Y. Zhou, X.Y. Li, D.N. Huang, Y. Zhu, Z.X. Wang, J.W. Tang, Covalent organic framework photocatalysts: structures and applications, Chem. Soc. Rev. 49 (12) (2020) 4135–4165.

[38] H. Zhong, R.J. Sa, H.W. Lv, S.L. Yang, D.Q. Yuan, X.C. Wang, R.H. Wang, Covalent organic framework hosting metalloporphyrin-based carbon dots for visible-light-driven selective CO_2 reduction, Adv. Funct. Mater. 30 (35) (2020) 8.

[39] W.Q. Li, X.F. Huang, T.W. Zeng, Y.H.A. Liu, W.B. Hu, H. Yang, Y.B. Zhang, K. Wen, Thiazolo 5,4-d thiazole-based donor-acceptor covalent organic framework for sunlight-driven hydrogen evolution, Angew. Chem. Int. Ed. 60 (4) (2021) 1869–1874.

[40] S.B. Jin, X.S. Ding, X. Feng, M. Supur, K. Furukawa, S. Takahashi, M. Addicoat, M. E. El-Khouly, T. Nakamura, S. Irle, S. Fukuzumi, A. Nagai, D.L. Jiang, Charge dynamics in a donor-acceptor covalent organic framework with periodically ordered bicontinuous heterojunctions, Angew. Chem. Int. Ed. 52 (7) (2013) 2017–2021.

[41] S.B. Jin, M. Supur, M. Addicoat, K. Furukawa, L. Chen, T. Nakamura, S. Fukuzumi, S. Irle, D.L. Jiang, Creation of superheterojunction polymers via direct polycondensation: segregated and bicontinuous donor-acceptor pi-columnar arrays in covalent organic frameworks for long-lived charge separation, J. Am. Chem. Soc. 137 (24) (2015) 7817–7827.

[42] K. Li, W.D. Zhang, Creating graphitic carbon nitride based donor-pi-acceptor-pi-donor structured catalysts for highly photocatalytic hydrogen evolution, Small 14 (12) (2018) 12.

[43] H.H. Ou, X.R. Chen, L.H. Lin, Y.X. Fang, X.C. Wang, Biomimetic donor-acceptor motifs in conjugated polymers for promoting exciton splitting and charge separation, Angew. Chem. Int. Ed. 57 (28) (2018) 8729–8733.

[44] Y.F. Zhi, S. Ma, H. Xia, Y.M. Zhang, Z. Shi, Y. Mu, X.M. Liu, Construction of donor-acceptor type conjugated microporous polymers: A fascinating strategy for the development of efficient heterogeneous photocatalysts in organic synthesis, Appl. Catal. B Environ. 244 (2019) 36–44.

[45] W. Zhou, Z.C. Hu, F. Huang, W. Hong, X.D. Chen, Metal-free hydrophilic D-A conjugated polyelectrolyte dots/g-C3N4 nanosheets heterojunction for efficient and irradiation-stable water-splitting photocatalysis, Appl. Catal. B Environ. 270 (2020) 9.

[46] C.Z. Li, J.L. Liu, H. Li, K.F. Wu, J.H. Wang, Q.H. Yang, Covalent organic frameworks with high quantum efficiency in sacrificial photocatalytic hydrogen evolution, Nat. Commun. 13 (1) (2022) 9.

[47] M. Calik, F. Auras, L.M. Salonen, K. Bader, I. Grill, M. Handloser, D.D. Medina, M. Dogru, F. Lobermann, D. Trauner, A. Hartschuh, T. Bein, Extraction of photogenerated electrons and holes from a covalent organic framework integrated heterojunction, J. Am. Chem. Soc. 136 (51) (2014) 17802–17807.

[48] Q.B. Liao, W.T. Xu, X. Huang, C. Ke, Q. Zhang, K. Xi, J. Xie, Donor-acceptor type 4 +3 covalent organic frameworks: sub-stoichiometric synthesis and photocatalytic application, Sci. China-Chem. 63 (5) (2020) 707–714.

[49] Y.P. Yuan, L.W. Ruan, J. Barber, S.C.J. Loo, C. Xue, Hetero-nanostructured suspended photocatalysts for solar-to-fuel conversion, Energy Environ. Sci. 7 (12) (2014) 3934–3951.

[50] X. Wang, X. Ding, T. Wang, K. Wang, Y. Jin, Y. Han, P. Zhang, N. Li, H. Wang, J. Jiang, Two-dimensional porphyrin-based covalent organic framework with enlarged inter-layer spacing for tunable photocatalytic CO_2 reduction, ACS Appl. Mater. Interfaces 14 (2022) 41122–41130.

[51] Y.Z. Chen, A.X. Li, Z.H. Huang, L.N. Wang, F.Y. Kang, Porphyrin-based nanostructures for photocatalytic applications, Nanomaterials 6 (3) (2016) 17.

[52] M.E. Cinar, T. Ozturk, Thienothiophenes, dithienothiophenes, and thienoacenes: syntheses, oligomers, polymers, and properties, Chem. Rev. 115 (9) (2015) 3036–3140.

[53] S. Topal, G. Suna, P. Ulukan, E. Sezer, T. Ozturk, Synthesis and optoelectronic and charge storage characterizations of conducting polymers based on tetraphenylethylene and thienothiophenes, Electrochim. Acta 392 (2021) 10.

[54] N. Keller, M. Calik, D. Sharapa, H.R. Soni, P.M. Zehetmaier, S. Rager, F. Auras, A. C. Jakowetz, A. Gorling, T. Clark, T. Bein, Enforcing extended porphyrin J-aggregate stacking in covalent organic frameworks, J. Am. Chem. Soc. 140 (48) (2018) 16544–16552.

[55] Q. Wu, M.J. Mao, Q.J. Wu, J. Liang, Y.B. Huang, R. Cao, Construction of donor-acceptor heterojunctions in covalent organic framework for enhanced CO_2 electroreduction, Small 17 (22) (2021) 8.

[56] B. Ravel, M. Newville, ATHENA, ARTEMIS, HEPHAESTUS: data analysis for X-ray absorption spectroscopy using IFEFFIT, J. Synchrotron Radiat. 12 (2005) 537–541.

[57] Q. Wu, R.K. Xie, M.J. Mao, G.L. Chai, J.D. Yi, S.S. Zhao, Y.B. Huang, R. Cao, Integration of strong electron transporter tetrathiafulvalene into metalloporphyrin-based covalent organic framework for highly efficient electroreduction of CO_2, ACS Energy Lett. 5 (3) (2020) 1005–1012.

[58] S. Xie, Q. Zhang, G. Liu, Y. Wang, Photocatalytic and photoelectrocatalytic reduction of CO_2 using heterogeneous catalysts with controlled nanostructures, Chem. Commun. 52 (1) (2016) 35–59.

[59] W. Zhong, R. Sa, L. Li, Y. He, L. Li, J. Bi, Z. Zhuang, Y. Yu, Z. Zou, A covalent organic framework bearing single Ni sites as a synergistic photocatalyst for selective photoreduction of CO_2 to CO, J. Am. Chem. Soc. 141 (2019) 7615–7621.

[60] H.B. Zhang, J. Wei, J.C. Dong, G.G. Liu, L. Shi, P.F. An, G.X. Zhao, J.T. Kong, X. J. Wang, X.G. Meng, J. Zhang, J.H. Ye, Efficient visible-light-driven carbon dioxide reduction by a single-atom implanted metal-organic framework, Angew. Chem. Int. Ed. 55 (46) (2016) 14308–14312.

[61] C. Gao, S.M. Chen, Y. Wang, J.W. Wang, X.S. Zheng, J.F. Zhu, L. Song, W.K. Zhang, Y.J. Xiong, Heterogeneous single-atom catalyst for visible-light-driven high-turnover CO_2 reduction: the role of electron transfer, Adv. Mater. 30 (13) (2018) 9.

[62] W. Liu, X. Li, C. Wang, H. Pan, W. Liu, K. Wang, Q. Zeng, R. Wang, J. Jiang, A scalable general synthetic approach toward ultrathin imine-linked two-dimensional covalent organic framework nanosheets for photocatalytic CO_2 reduction, J. Am. Chem. Soc. 141 (43) (2019) 17431–17440.

[63] S. Jin, X. Ding, X. Feng, M. Supur, K. Furukawa, S. Takahashi, M. Addicoat, M.E. El-Khouly, T. Nakamura, S. Irle, S. Fukuzumi, A. Nagai, D. Jiang, Charge dynamics in a donor–acceptor covalent organic framework with periodically ordered bicontinuous heterojunctions, Angew. Chem. Int. Ed. 52 (7) (2013) 2017–2021.

[64] J. Lv, Y.-X. Tan, J. Xie, R. Yang, M. Yu, S. Sun, M.-D. Li, D. Yuan, Y. Wang, Direct solar-to-electrochemical energy storage in a functionalized covalent organic framework, Angew. Chem. Int. Ed. 57 (39) (2018) 12716–12720.

[65] S.Y. Wang, X. Hai, X. Ding, S.B. Jin, Y.G. Xiang, P. Wang, B. Jiang, F. Ichihara, M. Oshikiri, X.G. Meng, Y.X. Li, W. Matsuda, J. Ma, S. Seki, X.P. Wang, H. Huang, Y. Wada, H. Chen, J.H. Ye, Intermolecular cascaded pi-conjugation channels for electron delivery powering CO_2 photoreduction, Nat. Commun. 11 (1) (2020) 9.
[66] Y.G. Xiang, W.B. Dong, P. Wang, S.Y. Wang, X. Ding, F. Ichihara, Z. Wang, Y. Wada, S.B. Jin, Y.X. Weng, H. Chen, J.H. Ye, Constructing electron delocalization channels in covalent organic frameworks powering CO_2 photoreduction in water, Appl. Catal. B Environ. 274 (2020) 8.
[67] Y.N. Gong, W. Zhong, Y. Li, Y. Qiu, L. Zheng, J. Jiang, H.L. Jiang, Regulating photocatalysis by spin-state manipulation of cobalt in covalent organic frameworks, J. Am. Chem. Soc. 142 (2020) 16723–16731.
[68] T. Skorjanc, D. Shetty, M.E. Mahmoud, F. Gándara, J.I. Martinez, A.K. Mohammed, S. Boutros, A. Merhi, E.O. Shehayeb, C.A. Sharabati, P. Damacet, J. Raya, S. Gardonio, M. Hmadeh, B.R. Kaafarani, A. Trabolsi, Metallated isoindigo-porphyrin covalent organic framework photocatalyst with a narrow band gap for efficient CO_2 conversion, ACS Appl. Mater. Interfaces 14 (2022) 2015–2022.
[69] G. Kresse, J. Furthmuller, Efficient iterative schemes for ab initio total-energy calculations using a plane-wave basis set, Phys. Rev. B. 54 (16) (1996) 11169–11186.
[70] J. Tomasi, B. Mennucci, R. Cammi, Quantum mechanical continuum solvation models, Chem. Rev. 105 (8) (2005) 2999–3093.